DOI: 10.13009/EUCASS2022-7331
9TH EUROPEAN CONFERENCE FOR AERONAUTICS AND SPACE SCIENCES (EUCASS)

Simulation of plasmas for electric propulsion using the energy-conserving semi-implicit PIC scheme

Pietro Parodi[⋆‡†]*, Giovanni Lapenta*[‡] *and Thierry Magin*[⋆]
[⋆]*von Karman Institute for Fluid Dynamics*
Waterloosesteenweg 72, B-1640 Sint-Genesius-Rode, Belgium
[‡]*Department of Mathematics, KU Leuven*
Department of Mathematics, B-3000 Leuven, Belgium
pietro.parodi@vki.ac.be · giovanni.lapenta@kuleuven.be · thierry.magin@vki.ac.be
[†]Corresponding author

Abstract

Simulation of plasmas for applications such as space electric propulsion, nuclear fusion, or heliophysics phenomena, is a complex task because of two reasons: first, the size of interest of the system is usually comparable to the collisional length scale because of the low pressure. The result is that velocity distributions are not always at equilibrium. Secondly, the length and time scales of interest are typically much larger than the natural length and time scales of the plasma, which are dictated by the light electrons. This can make simulations extremely expensive. Using particle methods, in particular the hybrid Particle-in-Cell – Direct Simulation Monte Carlo (PIC-DSMC) method, allows to solve the first problem, since phase space can be efficiently represented using computational particles. In this work, we show how energy conserving semi-implicit PIC schemes can substantially mitigate the second problem. We will show this using representative 1D simulations of a plasma slab expanding into vacuum. Then, we will present an unstructured Finite Element discretization of the energy conserving scheme in 2D.

1. Introduction

Orbiting platforms for Earth Observation and radio communication may benefit from flying at a lower altitude than traditional platforms,[13] in the so-called Very Low Earth Orbit (VLEO), at altitudes below 250 km. At these altitudes, the residual atmosphere causes a drag force on spacecraft, which would make it de-orbit in a matter a days if not compensated with thrust from an engine. If stored propellants are used, spacecraft lifetime is strongly limited by the amount of propellant on board. Recently, studies focused on a concept called Air-Breathing Electric Propulsion,[1,13–15] which proposes to collect the residual atmospheric molecules through an intake and use them as propellant in an electric thruster.

Ground testing of such propulsion systems is a complex task which requires recreating the orbital flow conditions on ground. The low pressure environment can be achieved only in a high-vacuum facility, and the flow of fast particles ($\approx$ 8 km/s) using a plasma source with an appropriate system for ion acceleration, which we call Particle Flow Generator (PFG). The alternative of gasdynamic acceleration in a converging-diverging nozzle has been explored before,[7] but generating a flow of sufficient diameter and Mach number does not seem achievable due to the low mass flow rate and pressure required. A Low-Density Facility is being constructed at VKI, where a PFG will generate the flow. Simulation is necessary both for the design of hardware and the experiments, but also for the interpretation of the experimental results. Therefore, our focus is the simulation of the PFG and the plasma flow it produces. The plasma involved in this application has parameters typical of laboratory and electric propulsion plasmas. The Knudsen number, which is the ratio of characteristic dimension and molecular mean free path, is in the range Kn$\approx$ 0.1–10. This means that a high degree of nonequilibrium is present, but gas phase collisions are still relevant. Electron number density is in the range 10^{13}–10^{17} m^{-3}, with temperatures of the order a few eV. Ions and neutrals are relatively cold, typically below 1000 K. Finally, plasma current densities are low enough that the induced magnetic field is insignificant, meaning that the electrostatic approximation can be safely adopted.

A fluid approach would not be appropriate for the simulation of the plasma in such conditions because of the high degree of translational nonequilibrium. Particle methods, on the other hand, can efficiently represent the six-dimensional *phase space* of 3D particle positions and 3D particle velocities in nonequilibrium. Such methods have

DOI: 10.13009/EUCASS2022-7331

been independently developed for collisional gases and for collisionless plasmas, under the names Direct Simulation Monte Carlo (DSMC),[3,4] and Particle-in-Cell (PIC).[8] The two methods can be merged in a hybrid PIC-DSMC code, since the underlying assumption of both is that computational particles represent a large number F_p of real particles. In DSMC, collision events instantaneously change the velocity of particle pairs undergoing the collision at each time step. In PIC, the velocity of charged particles is affected by the electromagnetic field computed on a computational grid, which itself takes into account charged particle currents or densities. We have recently started the development of the PIC-DSMC code Pantera at VKI.[12]

Simple electrostatic PIC schemes, like the one initially implemented in Pantera, typically employ an explicit discretization of Poisson's equation. With this scheme, numerical instabilities occur[8] if the cell size does not resolve the physical length scale of the plasma, the (electron) *Debye length* $\lambda_D = [\varepsilon_0 k T_e/(n_e q_e^2)]^{1/2}$, and the time step does not resolve the time scale of electron oscillations, dictated by the electron plasma frequency $\omega_{pe} = [n_e q_e^2/(m_e \varepsilon_0)]^{1/2}$. Here, ε_0 is the dielectric permittivity of vacuum, k is Boltzmann's constant, T_e and n_e are the electron temperature and number density, and q_e is the elementary charge. Unfortunately, the system scales of interest are, in many cases, much larger than the Debye length and the electron plasma period. This can render simulations extremely expensive, especially when two or three spatial dimensions are required. An interesting feature of some recently proposed implicit, energy-conserving schemes, is their ability to avoid the numerical instability called "Finite Grid Instability" in most practical simulation scenarios.[5,6,10] This empirical observation was subject of a thorough numerical analysis recently performed by Barnes and Chacón.[2] They reported a previously unidentified stability region when the Mach number for the electrons is less than $O(1)$. According to the authors, this condition is satisfied in plasmas where no significant charge separation is imposed by external fields. The explicit PIC algorithm currently constitutes the bottleneck for the efficient simulation of plasmas of our interest in Pantera. Therefore, in this work we will concentrate on the possible advantages of adopting an implicit, energy-conserving scheme.

In Section 2 we will introduce the physical model underlying the PIC method, and then present a Finite Element discretization of an explicit and of a semi-implicit PIC scheme. Then, in Section 3, we will study the effect of under-resolving physical electron length- and time scales to increase the efficiency of simulations. We will also present a test case for the 2D unstructured discretization of the PIC schemes implemented in Pantera.

2. Model and Methods

In this work we will present 1D and 2D simulations using an explicit and a semi-implicit PIC scheme. The 1D explicit scheme follows the classical textbook implementation, detailed, for instance, by Hockney and Eastwood.[8] The 1D implicit scheme is the electrostatic version of the energy-conserving semi-implicit method (ECSIM), which follows the implementation of Lapenta,[10] with the magnetic field set to zero. In this section, we illustrate the 2D Finite Element discretization of the explicit and semi-implicit electrostatic schemes on an unstructured grid.

2.1 Governing equations

We start from the Klimontovich form of the distribution function, where particles are points in phase space. As shown in Eq. (1), Dirac delta functions are used to represent the computational particles.

$$f_\alpha(\mathbf{x}, \mathbf{v}, t) = \sum_{p \in \alpha} F_p \, \delta\left[\mathbf{x} - \mathbf{x}_p(t)\right] \, \delta\left[\mathbf{v} - \mathbf{v}_p(t)\right] \tag{1}$$

Where the sum is performed over all computational particles of species α, which have position $\mathbf{x}_p$, velocity $\mathbf{v}_p$, and macroparticle weight F_p. We want to solve the Boltzmann equation with the Lorentz force term:

$$\frac{\partial f_\alpha}{\partial t} + \mathbf{v}_\alpha \cdot \nabla f_\alpha + \mathbf{a}_\alpha \cdot \nabla_\mathbf{v} f_\alpha = \left(\frac{\partial f_\alpha}{\partial t}\right)_{\text{coll}} \tag{2}$$

Where $\mathbf{a}_\alpha = \frac{q_\alpha}{m_\alpha}\mathbf{E}$ is the acceleration due to Lorentz force. In PIC, we solve for particle trajectories, which is equivalent to solving Boltzmann's equations with the method of characteristics:

$$\frac{\mathrm{d}\mathbf{v}_p}{\mathrm{d}t} = \frac{q_p}{m_p}\mathbf{E}(\mathbf{x}_p) + \sum_i \Delta\mathbf{v}_{p,i}\,\delta(t - t_i) \tag{3}$$

$$\frac{\mathrm{d}\mathbf{x}_p}{\mathrm{d}t} = \mathbf{v}_p \tag{4}$$

Notice that here, Newton's second law could also contain the effect of instantaneous collision events computed by the DSMC method, which change the particle's velocity by $\Delta\mathbf{v}_{p,i}$ at each collision instant t_i.

DOI: 10.13009/EUCASS2022-7331

Fields and particle positions are coupled through Maxwell's equations. Here, we consider the electro-quasi-static limit of Maxwell's equations, where the current induced magnetic field is considered negligible. Maxwell's equations reduce to the following:[9]

$$\nabla \cdot \mathbf{E} = \frac{\rho}{\varepsilon_0} \tag{5}$$

$$\nabla \times \mathbf{E} = 0 \tag{6}$$

$$\frac{\partial \rho}{\partial t} + \nabla \cdot \mathbf{J} = 0 \tag{7}$$

$$\nabla \times \mathbf{B}_1 = \mu_0 \left(\mathbf{J} + \varepsilon_0 \frac{\partial \mathbf{E}}{\partial t} \right) \tag{8}$$

Notice that the curl of the small magnetic field $\mathbf{B}_1$ in Ampère's law, Eq. (8), cannot be neglected in the equation, however, it can be neglected when computing the Lorentz force. Here, quantity ρ is the charge density, defined as:

$$\rho = \sum_{\alpha} \int_{\mathbb{R}^3} q_\alpha f_\alpha \, d\mathbf{v} = \sum_{p} q_p \delta \left[\mathbf{x} - \mathbf{x}_p(t) \right] \tag{9}$$

And $\mathbf{J}$ is the current density, defined as:

$$\mathbf{J} = \sum_{\alpha} \int_{\mathbb{R}^3} q_\alpha \mathbf{v} f_\alpha \, d\mathbf{v} = \sum_{p} q_p \mathbf{v}_p(t) \, \delta \left[\mathbf{x} - \mathbf{x}_p(t) \right] \tag{10}$$

Since the electric field is irrotational, we introduce the scalar potential ϕ, such that $\mathbf{E} = -\nabla\phi$. Then, Eq. (5) can be written as Poisson's equation:

$$\nabla^2 \phi = -\frac{\rho}{\varepsilon_0} \tag{11}$$

The discretization in space and time of a sufficient subset of these equations has been considered many times in literature for the construction of Particle-in-Cell schemes. We will now show an explicit discretization of Poisson's equation (11) and a semi-implicit discretization of the divergence of Eq. (8) on an unstructured grid using the Finite Element Method.

2.2 Unstructured explicit discretization of Poisson's equation

Using first order basis functions Ψ_i for the electric potential, this can be written as:

$$\phi(\mathbf{x}) = \sum_i \phi_i(t) \, \Psi_i(\mathbf{x}) \tag{12}$$

Multiplying Poisson's equation (11) with the basis function and integrating:

$$\int_\Omega \nabla^2 \phi \, \Psi_i \, \mathrm{d}S = -\frac{1}{\varepsilon_0} \int_\Omega \rho \, \Psi_i \, \mathrm{d}S \tag{13}$$

Using the Green-Ostrogradsky theorem:

$$\sum_j \phi_j \underbrace{\int_\Omega \nabla \Psi_j \cdot \nabla \Psi_i \, \mathrm{d}S}_{K^{ij}} = \underbrace{\int_{\Gamma_N} g \, \Psi_i \, \mathrm{d}\Gamma}_{\mathcal{N}} + \frac{1}{\varepsilon_0} \int_\Omega \rho \, \Psi_i \, \mathrm{d}S \tag{14}$$

Where $g = \frac{\partial \phi}{\partial \hat{\mathbf{n}}}$ is the Neumann boundary condition on the boundary Γ_N with normal $\hat{\mathbf{n}}$. Then we can write:

$$\sum_j K^{ij} \phi_j = \mathcal{N} + \frac{1}{\varepsilon_0} \sum_p q_p \Psi_i(\mathbf{x}_p) \tag{15}$$

Where we denoted with $\mathcal{N}$ the Neumann boundary term, and with K^{ij} the integrals of the basis functions. Notice that in 1D, this discretization would be equivalent to the common finite difference discretization with "cloud-in-cell" hat shape functions for the particles. With an explicit discretization in time, this becomes:

$$\sum_j K^{ij} \phi_j^n = \mathcal{N}^n + \frac{1}{\varepsilon_0} \sum_p q_p \Psi_i(\mathbf{x}_p^n) \tag{16}$$

DOI: 10.13009/EUCASS2022-7331

The electric field on the particles can then be written as

$$\mathbf{E}_p^n = \mathbf{E}^n(\mathbf{x}_p^n) = -\sum_i \phi_i^n \nabla\Psi(\mathbf{x}_p^n) \tag{17}$$

And particle position is advanced using the leapfrog scheme

$$\mathbf{v}_p^{n+\frac{1}{2}} = \mathbf{v}_p^{n-\frac{1}{2}} + \frac{q_p}{m_p}\mathbf{E}_p^n \Delta t \tag{18}$$

$$\mathbf{x}_p^{n+1} = \mathbf{x}_p^n + \mathbf{v}_p^{n+\frac{1}{2}} \Delta t \tag{19}$$

2.3 Unstructured semi-implicit discretization for energy conservation

We follow the work of Lapenta[10] to obtain a scheme that conserves energy exactly. Since we want to avoid solving for the current-induced magnetic field $\mathbf{B}_1$, we take the divergence of Ampère's equation (8):

$$\nabla \cdot \frac{\partial \mathbf{E}}{\partial t} + \frac{1}{\varepsilon_0}\nabla \cdot \mathbf{J} = 0 \tag{20}$$

Then, we substitute the definition of electric potential:

$$\frac{\partial}{\partial t}\left(\nabla^2\phi\right) - \frac{1}{\varepsilon_0}\nabla \cdot \mathbf{J} = 0 \tag{21}$$

We discretize this in time, considering the mid-step current as in the original ECSIM scheme:[10]

$$\nabla^2\phi^{n+1} - \nabla^2\phi^n - \frac{\Delta t}{\varepsilon_0}\nabla \cdot \bar{\mathbf{J}} = 0 \tag{22}$$

Where we denote with $\bar{A} = (A^n + A^{n+1})/2$ the mid-step average of quantity A. We can write:

$$\nabla^2\bar{\phi}^{n+1} - \nabla^2\phi^n - \frac{\Delta t}{2\varepsilon_0}\nabla \cdot \bar{\mathbf{J}} = 0 \tag{23}$$

Again, we perform the spatial discretization using the Finite Element method with linear basis functions $\phi(\mathbf{x}, t) = \sum_j \phi_j(t)\Psi_j(\mathbf{x})$, to obtain:

$$\sum_j \bar{\phi}_j \int_\Omega \nabla\Psi_i \cdot \nabla\Psi_j \, dS - \sum_j \phi_j^n \int_\Omega \nabla\Psi_i \cdot \nabla\Psi_j \, dS - \int_{\Gamma_N} \frac{\partial(\bar{\phi} - \phi^n)}{\partial\hat{\mathbf{n}}}\Psi_i \, d\Gamma - \frac{\Delta t}{2\varepsilon_0}\int_\Omega \bar{\mathbf{J}} \cdot \nabla\Psi_i \, dS = 0 \tag{24}$$

Substituting the definition of current, Eq. (10):

$$\sum_c \sum_j \bar{\phi}_j K_c^{ij} - \sum_c \sum_j \phi_j^n K_c^{ij} - \frac{\Delta t}{2\varepsilon_0}\sum_c \sum_{p\in c} q_p \bar{\mathbf{v}}_p \cdot \nabla\Psi_i(\bar{\mathbf{x}}_p) = 0 \tag{25}$$

Where we've dropped the Neumann term for simplilcity. This is an implicit equation coupled to the motion of the particles, since the future electric potential depends on the future particle velocities. If the leapfrog particle mover is used, the solution can be obtained by writing explicitly the particle response through mass factors and solving the linear system directly, hence the "semi-implicit" nature. We can then obtain:

$$\sum_c \sum_j \bar{\phi}_j K_c^{ij} + \sum_c \sum_j \bar{\phi}_j K_c^{ij} \frac{\Delta t}{2\varepsilon_0}\sum_{p\in c} \frac{q_p^2 \Delta t}{2 m_p A_\Delta} = \frac{\Delta t}{2\varepsilon_0}\sum_c \sum_{p\in c} q_p \mathbf{v}_p^n \cdot \nabla v_i(\mathbf{x}_p^{n+\frac{1}{2}}) + \sum_c \sum_j \phi_j^n K_c^{ij} \tag{26}$$

We can thus write for each internal node i:

$$\sum_c \left[(1 + M_c)\sum_j \bar{\phi}_j K_c^{ij}\right] = \sum_c \left[\frac{\Delta t}{2\varepsilon_0} J_c^i + \sum_j \phi_j^n K_c^{ij}\right] \tag{27}$$

Where the particle response to the electric field is contained in:

$$M_c = \frac{\Delta t^2}{4\varepsilon_0 V_c}\sum_{p\in c} \frac{q_p^2}{m_p} \tag{28}$$

DOI: 10.13009/EUCASS2022-7331

And the current is computed as:

$$J_c^i = \sum_{p \in c} q_p \mathbf{v}_p^n \cdot \nabla \Psi_i(\mathbf{x}_p^{n+\frac{1}{2}}) \tag{29}$$

We show in the appendix that using this scheme, the total energy, defined as:

$$\mathcal{E} = \sum_p m_p \left|\mathbf{v}_p\right|^2 + \frac{1}{2}\varepsilon_0 \int_\Omega |\mathbf{E}|^2 \, dS, \tag{30}$$

is conserved exactly. This leads to the interesting stability properties of this scheme. Notice that charge is not conserved exactly by the scheme we derived. This means that, even if Poisson's equation is satisfied initially, it will not be necessarily satisfied at later time. The reason is the way the current is computed does not account for the real displacement of the charges. Techniques have been devised to decrease this error or eliminate it completely, at the expense of additional complexity and computational cost. See for instance the work of Chen *et al.*[5]

3. Results

3.1 Cartesian 1D test case: plasma slab expanding into vacuum

In this section we will compare the explicit and semi-implicit schemes using the test case of 1D expansion of plasma in a periodic domain. The plasma parameters in this test case aim at being representative of those often encountered in electric propulsion.

The domain is discretized using a uniform Cartesian mesh. It is initialized with quasineutral plasma at a density $n = 5 \times 10^{16}$ m^{-3}. Ions are at a temperature $T_i = 300$ K, and electrons are at $T_e = 1$ eV. The physical size of the domain is fixed at 2000 λ_D. For the first cases, 1E and 1I, we start from scale-resolving simulations with 4000 cells, which correspond to cell sizes of $0.5\lambda_D$. The time step is initially set at a value that resolves the electron plasma frequency ω_{pe}, and such that electrons do not cross more than one cell at a time. The latter condition is achieved in practice by imposing $\Delta t < \Delta x / v_{\text{th},e}$, where $v_{\text{th},e} = [8kT_e/(\pi m_e)]^{1/2}$ is the thermal velocity of electrons. In all simulations, we use a particle weight of 4×10^9, for a total of 831 136 simulated particles.

First, we show in Figure 1 that the semi-implicit scheme conserves energy to machine precision (or the precision of the direct linear solver), regardless of grid size or time step. Conversely, in all simulations using the explicit scheme, the total energy increases in time. When the Debye length and electron plasma frequency are well resolved (case 1E), the increase can be considered acceptable, especially for short simulations.

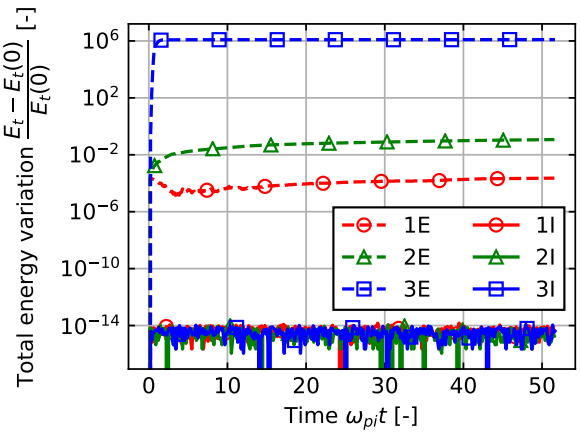

Figure 1: Evolution of the variation of total energy in the simulation for all cases considered.

Figures 2a and 2b show instantaneous electric field, ion velocity and ion density at instants $\omega_{pi}t = 22.08$ and 51.52. In the figures, we compare the solutions to the two-fluid solution obtained by Mora.[11] The author solved the ion continuity and momentum equations coupled to Poisson's equation and Boltzmann's relation for isothermal electrons. Following Mora,[11] results are nondimensionalized using a reference electric field $E_0 = [n_0 kT_e/\varepsilon_0]^{1/2}$, the ion acoustic velocity $c_s = [kT_e/m_i]^{1/2}$, and the Debye length in the bulk of the plasma, $\lambda_D = [\varepsilon_0 kT_e/(n_0 q_e^2)]^{1/2}$. The results of the

DOI: 10.13009/EUCASS2022-7331

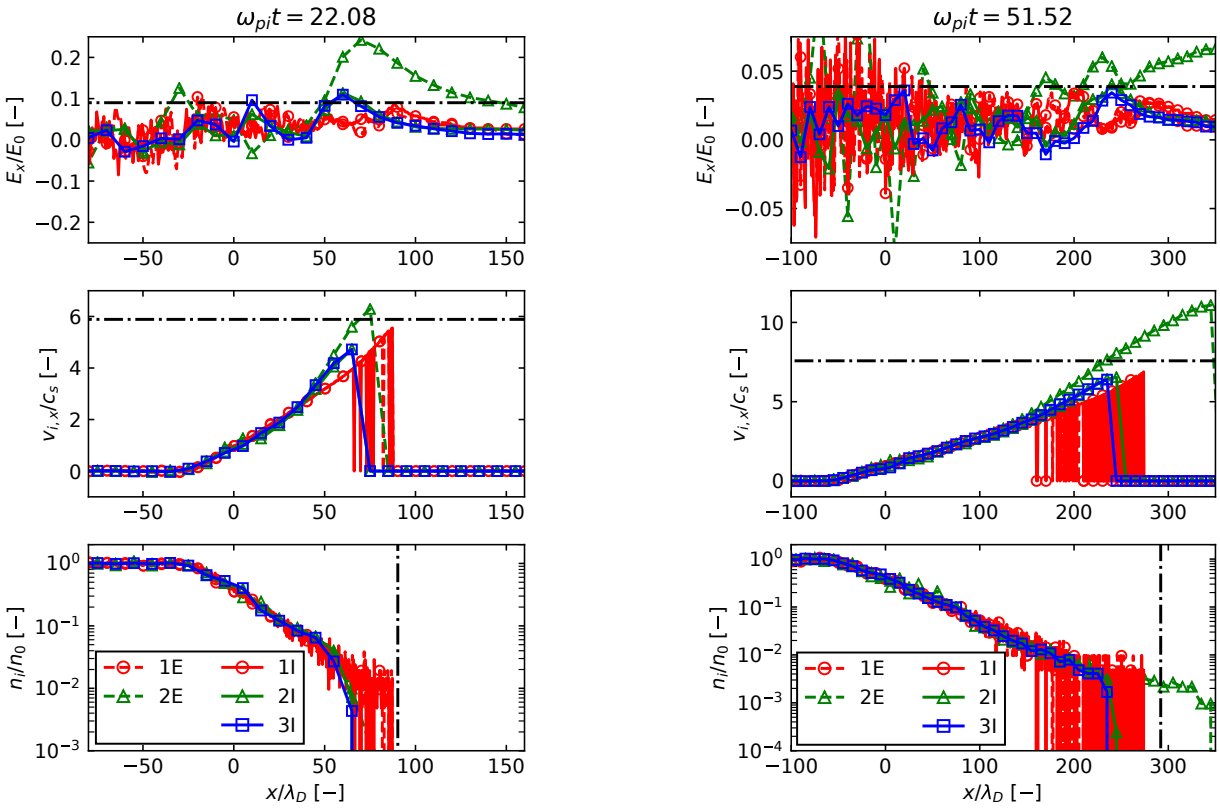

(a) (b)

Figure 2: Curves of electric field, ion drift velocity, and ion density for the cases listed in Table 1 at instants (a) $\omega_{pi}t = 22.08$, and (b) $\omega_{pi}t = 51.52$. For case 3E the simulation is numerically unstable and not shown here. The peak electric field, velocity and position of the ion front from the fluid solution of Mora[11] are shown with dot-dashed lines. Quantities $E_0 = [n_0 k T_e/\varepsilon_0]^{1/2}$, $c_s = [kT_e/m_i]^{1/2}$, and $\lambda_D = [\varepsilon_0 k T_e/(n_0 q_e^2)]^{1/2}$ are used for nondimensionalization.

explicit and implicit scheme in this well-resolving case are almost identical, and match very well with the peak electric field, ion front velocity and position predicted by the fluid solution, shown with the dot-dashed lines.

If now we wish to decrease the computational cost, we need to coarsen the grid and increase the time step. The latter is typically not possible without the former, since we are bound by the cell crossing constraint:

$$(\omega_{pe}\Delta t) \propto \left(\frac{\Delta x}{\lambda_D}\right) \Big/ \left(\frac{\Delta x}{v_{th,e}\Delta t}\right) \tag{31}$$

As made clear by the expression, often we cannot increase $\omega_{pe}\Delta t$ unless we also increase $\Delta x/\lambda_D$, since the last term cannot be decreased below a certain value.

Therefore, we perform simulations 2E and 2I with a coarsened grid. Since the ambipolar expansion of a plasma occurs on length scales of the order of λ_D, we must address the effect of coarsening the simulation grid on the accuracy of the results. The increased cell size exceeds the stability limit of the explicit scheme (case 2E). In fact, Figure 1 shows that the total energy increases by 12% for this simulation. Figures 2a and 2b show an abnormal value of the peak electric field and ion front velocity. These results give a hint to why the explicit scheme is typically used only well within its stability region. The implicit scheme (case 2I) behaves better, with no abnormal electric field peak. The only difference is the position of the ion front, which trails behind the value of the refined simulations and the fluid solution, as can be seen by the density plots. This may be explained by the lack of resolution of the sharp ion front region in the initial instants of the simulation. The effect may be mitigated by a local refinement of the grid at the initial plasma-vacuum interface. Nonetheless, the simulation is stable, and captures well the much more refined solutions.

At this point, we are also free to increase the time step above the electron plasma frequency ω_{pe}, since the cell-crossing constraint is relaxed. As apparent in Figure 1, it is not possible to perform this simulation with the explicit scheme (case 3E) because its stability criteria are not respected. When using the implicit scheme (case 3I), on the other hand, increasing the time step does not degrade the solution with respect to case 2I, in fact the two solutions overlap

DOI: 10.13009/EUCASS2022-7331

in Figures 2a and 2b. This is probably because, as is often the case, the phenomenon of interest does not depend directly on the electron time scale, but rather on the ion time scale ω_{pi}^{-1} which is much larger and still well resolved. The parameters for all cases are summarized in Table 1.

The phase space solution for cases 1E, 2E, and 3I at time $\omega_{pi}t = 22.08$ can be compared in Figure 3. For clarity, these show the phase space only in correspondence of the plasma-vacuum interface, $x \in [-150, 150]\lambda_D$. The velocities are nondimensionalized with the thermal velocities of electrons and ions. Notice that in case 3I (Figure 3c), electrons and ions do not shown any sign of instability. As indicated by the previous plots, a slight difference can be seen in the expanding ion population, where front position and velocity are smaller than in simulation 1E. Remarkably, the expansion region at this instant is resolved using only about 10 cells.

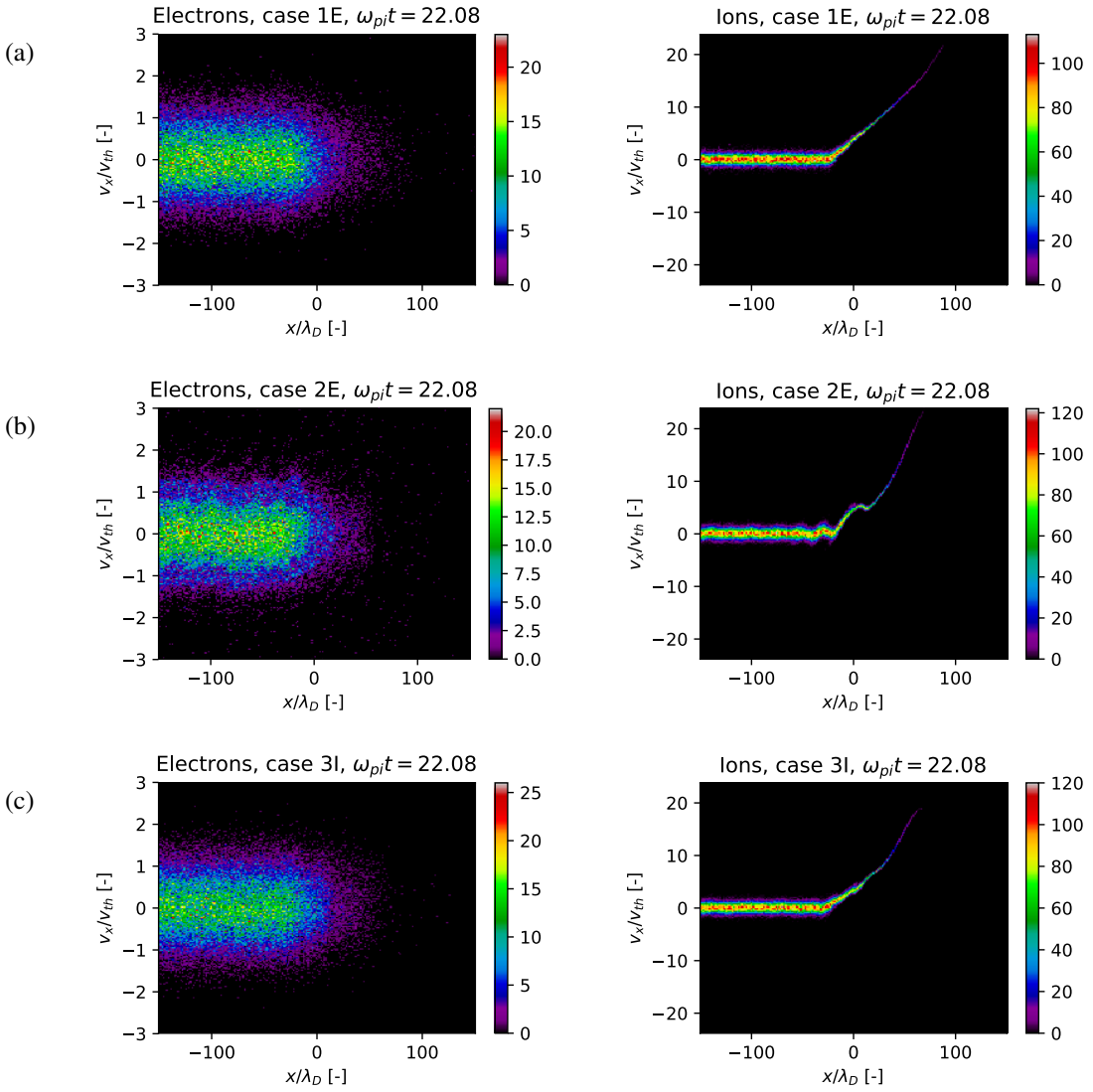

Figure 3: Electron and ion phase space in correspondence of the ion front for cases (a) 1E, (b) 2E, and (c) 3I, at instant $\omega_{pi}t = 22.08$. The velocities are nondimensionalized with the thermal velocities. The plots are obtained as a 2D histogram of position and velocity of all particles in the simulation at this instant. The color scale shows the number of particles in a given interval of the histogram. The first signs of numerical instability are visible in case 2E. Conversely, in case 3I, where the time step is 50 times smaller but the implicit scheme is used, electrons and ions do not shown signs of instability. Case 3I shows a difference in the expanding ion population, where front position and velocity in simulation trail behind those of the well resolved simulation 1E, as already shown in Figure 2a. Remarkably, however, the expansion region in case 3I is resolved using only 10 cells.

The simulations were performed on 16 parallel MPI processes on an AMD Ryzen Threadripper 1950X processor. The computational time required for the simulations is shown in Table 1. Generally, the implicit scheme is more

DOI: 10.13009/EUCASS2022-7331

Table 1: Summary of main numerical parameters for the 1D simulations of plasma expansion into vacuum using the explicit and implicit scheme. The wall clock time for the simulations is reported in the last column.

Case	$\mathbf{\Delta x}/\lambda_\mathbf{D}$ [-]	$\omega_\mathbf{pe}\mathbf{\Delta t}$ [-]	$\frac{\mathbf{\Delta x}}{\mathbf{v_{th,e}\Delta t}}$ [-]	**scheme**	**time** s
1E	0.5	0.063	5.0	explicit	876
2E	10	0.063	100	explicit	731
3E	10	3.15	2.0	explicit	83
1I	0.5	0.063	5.0	implicit	9363
2I	10	0.063	100	implicit	774
3I	10	3.15	2.0	implicit	98

demanding for the same set of parameters, since it requires the computation of the mass factors and the factorization of the linear system matrix at each timestep. For the explicit scheme, instead, this factorization is performed only once at the beginning of the simulation. However, the implicit scheme still allows to obtain a sufficiently accurate simulation at least 9× faster than the well resolved explicit simulation (case 1E). Notice that here we've kept the number of particles constant, while they could have been reduced proportionally to the number of cells, resulting in a further speedup. This speedup is expected to be exponentially more advantageous for 2D and 3D simulations, as discussed by Chen *et al.*[5]

The present test cases were limited to a periodic domain. In the following section, we will present the case of a 2D simulation with boundaries.

3.2 Unstructured 2D test case: cylindrical Langmuir probe

Given the possible advantages of adopting an energy-conserving implicit scheme, we implemented the Finite Element discretization illustrated in Section 2.3 in Pantera. As a test case, we simulate the plasma sheath forming around a cylindrical conductor, remnant of a cyindrical Langmuir probe. The discretized domain is shown in Figure 4. The internal circular edge "c" represents the conductor. It has a radius $R_1 = 0.25$ m, and Dirichlet boundary conditions $\phi = \phi_w = 0$ are applied. Edges "s" have Neumann boundary conditions $\partial\phi/\partial\hat{\mathbf{n}} = 0$ and specular reflection for particles. The outer circular edge "i" has radius $R_2 = 1.5$ m. We inject electrons and argon ions from the outer boundary at $T_e = T_i = 300$ K and $n_e = n_i = n_0 = 5 \times 10^9$ m^{-3}. The Debye length in these conditions is $\lambda_{D_0} = 0.017$ m. The mesh of Figure 4a resolves this length. We perform a simulation using this mesh and the explicit scheme, in order to obtain a reference solution. Then, we perform a simulation with mesh b) using the implicit method. We also compare the PIC solutions with the solution to the following system of plasma fluid equations in cylindrical coordinates: ion continuity (32), ion momentum (33), Poisson's equation (34), and Boltzmann's relation for isothermal electrons (35):

$$\frac{\mathrm{d}n_i}{\mathrm{d}r} = -\frac{n_i}{r} - \frac{n_i}{v_i}\frac{\mathrm{d}v_i}{\mathrm{d}r} \tag{32}$$

$$\frac{\mathrm{d}v_i}{\mathrm{d}r} = -\frac{1}{v_i}\frac{q_e}{m_i}\frac{\mathrm{d}\phi}{\mathrm{d}r} \tag{33}$$

$$\frac{\mathrm{d}^2\phi}{\mathrm{d}r^2} + \frac{1}{r}\frac{\mathrm{d}\phi}{\mathrm{d}r} = -\frac{q_e}{\varepsilon_0}(n_i - n_e) \tag{34}$$

$$n_e = n_0 \exp\left[\frac{q_e(\phi - \phi_r)}{kT_e}\right] \tag{35}$$

The equations are integrated with boundary conditions $\phi(R_2) = \phi_r$, $d\phi/dr(R_2) = 0$, $n_i(R_2) = n_e(R_2) = n_0$, and the balance of electron and ion fluxes at the conductor: $1/4 n_e(R_1)[8kT_e/(\pi m_e)]^{1/2} = -n_i(R_1)v_i(R_1)$. We don't expect these solutions to match exactly because the fluid equations do not take into account nonequilibrium. However, this simple fluid model should still capture the relevant features of the plasma sheath.

The results of these simulations are plotted in Figure 5. The figure shows the values of the species number density, the electric potential, and the radial velocity of ions as function of the radial coordinate. First, we note that the implicit solution is stable and matches well the explicit one, despite the Debye length not being resolved: $\Delta x \approx 2\lambda_{D_0}$ close to the inner boundary, and $\Delta x \approx 10\lambda_{D_0}$ close to the outer boundary. Expectedly, the fluid solution does not match exactly the PIC solutions, especially in terms of density profiles, probably because it does not capture kinetic effects. However, it shows that the size of the sheath, which is the region of charge non-neutrality, is well represented. A good agreement is found for the potential drop and ion velocity gain across the sheath. This simulation highlighted the fact

DOI: 10.13009/EUCASS2022-7331

that even a local refinement of the mesh for the resolution of the plasma sheath limits the global maximum time step that can be achieved. A possible solution to this problem is represented by substepping methods,[5,6] where particles are moved in small steps such that current is correctly deposited on the grid. This, however, would require nonlinear convergence of particles and fields.

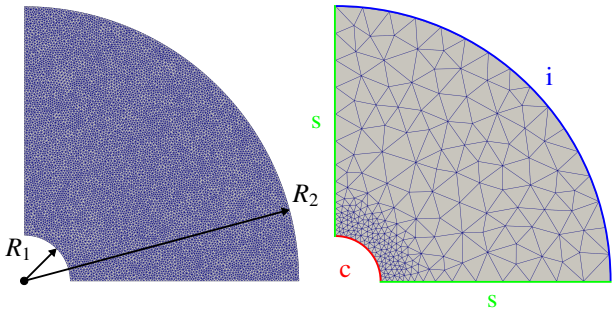

Figure 4: Unstructured meshes used for a) the explicit case, and b) the implicit case. Boundary conditions are indicated with c: conducting wall with fixed potential and particle deletion; s: Neumann condition for the potential and specular reflection for the particles; and i: fixed potential and particle injected at prescribed density and temperature. Mesh a) resolves the Debye length, while b) only resolves macroscopic gradients.

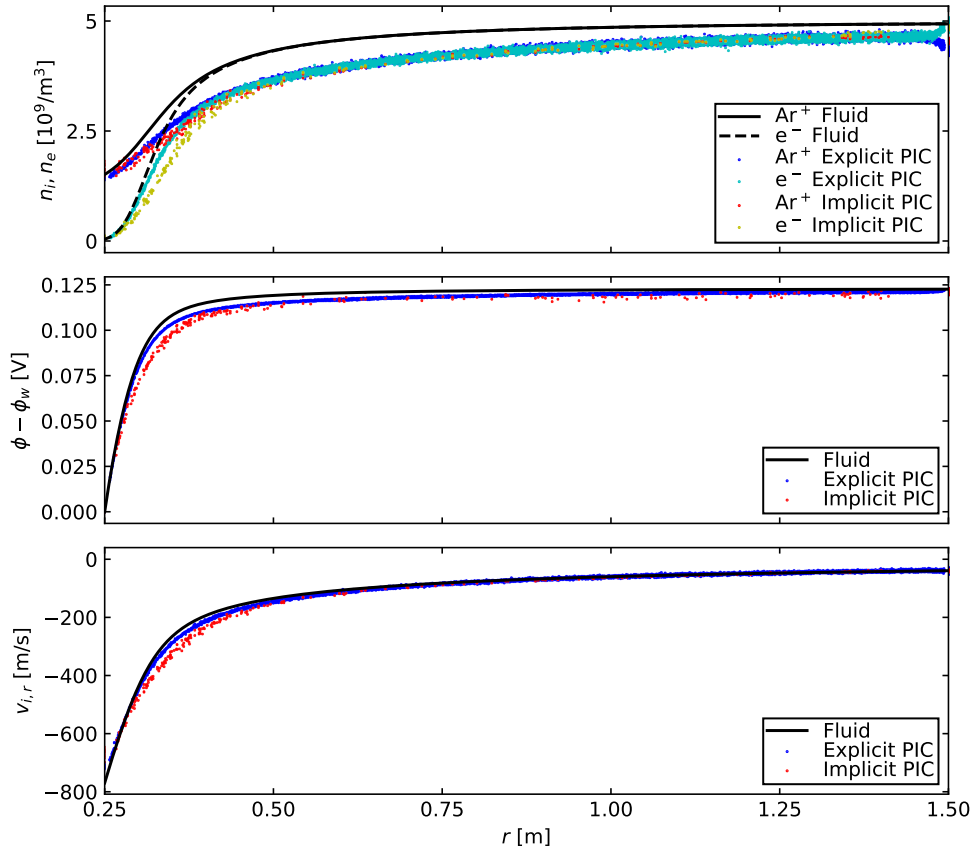

Figure 5: Cylindrical sheath solution using the explicit and the implicit schemes in PANTERA and the fluid equations (32)-(35). The panels show the plots of ion and electron number densities n_i, n_e, electric potential ϕ relative to the potential of the inner surface ϕ_w, and ion radial bulk velocity $v_{i,r}$. The points correspond to time-averaged cell or node values.

DOI: 10.13009/EUCASS2022-7331

4. Conclusion and Future Work

We have shown the advantages of adopting a semi-implicit PIC scheme for the simulation of plasmas of interest for applications such as electric propulsion. In the representative 1D simulations using both the explicit and the implicit schemes. The latter was able to give reasonably accurate results with a grid 20 times coarser and a time step 50 times larger than what needed by the explicit scheme. We recorded a speed-up of approximately one order of magnitude. Adopting an iterative solver such as GMRES may be more advantageous for the implicit scheme than the direct solver we are currently using, since factorization of the system matrix is computed at each time step.

We have successfully extended Pantera for the treatment of 2D unstructured meshes, and shown that this discretization retains the properties of the semi-implicit scheme of energy conservation and suppression of the finite grid instability. As future work, we will quantify the charge conservation error for relevant simulations, and explore nonlinearly converged schemes with particle substepping, which may be advantageous to achieve larger simulation time steps.

5. Acknowledgements

The research of PP is founded by an FWO Strategic Basic PhD fellowship (reference 1S24022N).

References

[1] T. Andreussi, G. Cifali, V. Giannetti, A. Piragino, E. Ferrato, A. Rossodivita, and M. Andrenucci. Development and Experimental Validation of a Hall Effect Thruster RAM-EP Concept. In *35th International Electric Propulsion Conference*, 2017.

[2] D.C. Barnes and L. Chacón. Finite spatial-grid effects in energy-conserving particle-in-cell algorithms. *Computer Physics Communications*, 258:107560, 2021.

[3] G. A. Bird. Approach to Translational Equilibrium in a Rigid Sphere Gas. *The Physics of Fluids*, 6(10):1518–1519, 1963.

[4] G. A. Bird. *Molecular Gas Dynamics and the Direct Simulation of Gas Flows*. Clarendon Press, 1994.

[5] G. Chen, L. Chacón, and D. C. Barnes. An Energy- and Charge-conserving, Implicit, Electrostatic Particle-in-Cell Algorithm. *Journal of Computational Physics*, 230(18):7018–7036, 2011.

[6] D. Eremin. An energy- and charge-conserving electrostatic implicit particle-in-cell algorithm for simulations of collisional bounded plasmas. *Journal of Computational Physics*, 452:110934, 2022.

[7] K. Fujita, T. Suzuki, and T. Ozawa. Development of a Pilot Model of Hypersonic Rarefied Wind-Tunnel. In *AIP Conference Proceedings*, volume 1333, pages 407–412, 2011.

[8] R. W. Hockney and J. W. Eastwood. *Computer Simulation Using Particles*. CRC Press, 1988.

[9] S. E. Kruger. The Three Quasistatic Limits of the Maxwell Equations. *arXiv:1909.11264v2*, 2019.

[10] G. Lapenta. Exactly energy conserving semi-implicit particle in cell formulation. *Journal of Computational Physics*, 334:349–366, 2017.

[11] P. Mora. Plasma Expansion into a Vacuum. *Physical Review Letters*, 90(18):185002, 2003.

[12] P. Parodi. Development of a hybrid PIC-DSMC solver for particle flow generators. Technical report, von Karman Institute for Fluid Dynamics, 2020.

[13] T. Schönherr, K. Komurasaki, F. Romano, B. Massuti-Ballester, and G. Herdrich. Analysis of Atmosphere-Breathing Electric Propulsion. *IEEE Transactions on Plasma Science*, 43(1):287–294, 2015.

[14] M. Tisaev, E. Ferrato, V. Giannetti, C. Paissoni, N. Baresi, A. Fabris, and T. Andreussi. Air-breathing electric propulsion: Flight envelope identification and development of control for long-term orbital stability. *Acta Astronautica*, 191:374–393, 2021.

[15] J. Virgili-Llop, P. Roberts, Z. Hao, L. Ramio, and V. Beauplet. Very Low Earth Orbit mission concepts for Earth Observation. Benefits and challenges. In *Reinventing Space Conference*, 2014.

DOI: 10.13009/EUCASS2022-7331

A. Proof of energy conservation for the unstructured discretization

The variation of kinetic energy of the particles in a time step is:

$$\Delta\mathcal{E}_p = \frac{1}{2}\sum_p m_p|\mathbf{v}_p^{n+1}|^2 - \frac{1}{2}\sum_p m_p|\mathbf{v}_p^{n}|^2 \tag{36}$$

While the variation in the energy stored in the electric field is:

$$\Delta\mathcal{E}_f = \frac{1}{2}\varepsilon_0\int_\Omega |\mathbf{E}^{n+1}|^2 dS - \frac{1}{2}\varepsilon_0\int_\Omega |\mathbf{E}^{n}|^2 dS \tag{37}$$

We will now prove that the total energy in the simulation is exactly conserved by the unstructured discretization of the ECSIM scheme in a periodic domain ($\Delta\mathcal{E}_p + \Delta\mathcal{E}_f = 0$). Since $|\mathbf{U}|^2 - |\mathbf{V}|^2 = (\mathbf{U}-\mathbf{V})\cdot(\mathbf{U}+\mathbf{V})$, we can write:

$$\Delta\mathcal{E}_p = \frac{1}{2}\sum_p m_p(\mathbf{v}_p^{n+1} - \mathbf{v}_p^{n})\cdot(2\mathbf{v}_{p,i}^{n+\frac{1}{2}}) \tag{38}$$

Substituting the particle mover, Eq. (18):

$$\Delta\mathcal{E}_p = \frac{1}{2}\sum_p m_p\left(\frac{q_p}{m_p}\bar{\mathbf{E}}_p\Delta t\right)\cdot(2\bar{\mathbf{v}}_p) \tag{39}$$

Substituting the definition of electric field as gradient of the potential and how it is applied to the particles, we obtain:

$$\Delta\mathcal{E}_p = \Delta t\sum_p\left(-\sum_j \bar{\phi}_j\nabla\Psi_j(\mathbf{x}_p^{n+\frac{1}{2}})\right)\cdot q_p\bar{\mathbf{v}}_p. \tag{40}$$

For the field energy, since $|\mathbf{U}|^2 - |\mathbf{V}|^2 = (\mathbf{U}-\mathbf{V})\cdot(\mathbf{U}+\mathbf{V})$, we can write:

$$\Delta\mathcal{E}_f = \frac{1}{2}\varepsilon_0\int_\Omega(\mathbf{E}^{n+1} - \mathbf{E}^{n})\cdot(2\mathbf{E}^{n+\frac{1}{2}})\,dS \tag{41}$$

Substituting the definition of potential

$$\Delta\mathcal{E}_f = \frac{1}{2}\varepsilon_0\int_\Omega\left(\nabla\phi^{n+1} - \nabla\phi^{n}\right)\cdot(2\nabla\bar{\phi})\,dS \tag{42}$$

Substituting $\bar{\phi} = (\phi^n + \phi^{n+1})/2$

$$\Delta\mathcal{E}_f = \frac{1}{2}\varepsilon_0\int_\Omega(2\nabla\bar{\phi} - 2\nabla\phi^{n})\cdot(2\nabla\bar{\phi})\,dS \tag{43}$$

splitting the integral

$$\Delta\mathcal{E}_f = 2\varepsilon_0\int_\Omega\nabla\bar{\phi}\cdot\nabla\bar{\phi}\,dS - 2\varepsilon_0\int_\Omega\nabla\phi^{n}\cdot\nabla\bar{\phi}_i\,dS \tag{44}$$

Using the global basis representation of the potential: $\phi(\mathbf{x}) = \sum_j\phi_j\Psi_j(\mathbf{x})$

$$\Delta\mathcal{E}_f = \sum_j 2\bar{\phi}_j\varepsilon_0\int_\Omega\nabla\bar{\phi}\cdot\nabla\Psi_j\,dS - \sum_j 2\bar{\phi}_j\varepsilon_0\int_\Omega\nabla\phi^{n}\cdot\nabla\Psi_j\,dS \tag{45}$$

Grouping terms

$$\Delta\mathcal{E}_f = \sum_j 2\bar{\phi}_j\varepsilon_0\left(\int_\Omega\nabla\bar{\phi}\cdot\nabla\Psi_j\,dS - \int_\Omega\nabla\phi^{n}\cdot\nabla\Psi_j\,dS\right) \tag{46}$$

Recognize our weak form, Eq. (24), between parentheses:

$$\Delta\mathcal{E}_f = \sum_j\bar{\phi}_j\Delta t\int_\Omega\bar{\mathbf{J}}\cdot\nabla\Psi_j\,dS \tag{47}$$

Substitute the definition of particle current

$$\Delta\mathcal{E}_f = \sum_j\bar{\phi}_j\Delta t\sum_p q_p\bar{\mathbf{v}}_p\cdot\nabla\Psi_j(\mathbf{x}_p^{n+\frac{1}{2}}) \tag{48}$$

Which by inspection is equal and opposite to the particle energy variation, Eq. (40), so that

$$\Delta\mathcal{E} = \Delta\mathcal{E}_p + \Delta\mathcal{E}_f = 0 \tag{49}$$

Notice that this is true only when the weak form is applied for all nodes, such as in a periodic domain, or with free boundary conditions with specular particle reflection.